PHYSICAL REVIEW E VOLUME 47, NUMBER 2 FEBRUARY 1993

Growth instability and pricking-fracture mechanism in smectic-*A* focal-conic nucleation

J. B. Fournier, M. Warenghem,* and G. Durand

Laboratoire de Physique des Solides, Université Paris-Sud, Bâtiment 510, F-91405 Orsay, France

(Received 24 July 1992; revised manuscript received 28 September 1992)

We show that smectic-*A* plates growing from the top of isotropic droplets are subject to an interfacial growth instability. This instability occurs before the static textural instability already known which produces focal conics in order to relax the smectic-*A*–isotropic surface energy. We study the growth instability and its relation with the tunneling through the barrier of the first-order static instability. We find that the focal conics nucleate on the nonlinearities of the growth instability through a fracture mechanism.

PACS number(s): 61.30.Jf, 47.35.+i

I. INTRODUCTION

Smectic-*A* liquid crystals [1] are made of parallel rodlike molecules piled inside monomolecular liquid layers to which the molecules are oriented normally. The smectic layers can be easily curved by external forces, but they essentially remain equidistant. This causes the creation of pairs of linear defects, an ellipse and the conjugated confocal hyperbola, which are the common curvature centers of the smectic layers. These defects, called *focal conics* [2], are the characteristic macroscopic defects of smectics.

It has recently been demonstrated [3] that smectic-*A* plates growing from the top of isotropic droplets are intrinsically unstable. Above a thickness threshold, they are subject to a textural instability producing focal conics. According to the model of Ref. [3], these focal conics are stabilized by the contact with the isotropic phase, where they relax the surface-energy anisotropy. The same mechanism also explains the presence of focal conics inside the smectic-*A* germs, the so-called Grandjean *bâtonnets* [2] nucleating inside the isotropic bulk [4]. The smectic-*A* plates' instability was described as a potential instability; however, a dependence of the instability threshold with respect to the smectic growth velocity was reported [3].

In this paper, we study the *growth* of the above-described smectic-*A* plates, in order to elucidate which part of the growth dynamics plays in the nucleation mechanism of their stable focal conics. In Sec. II we describe our experimental setup. In Sec. III we report the observation of a growth instability of the smectic-*A*–isotropic interface, revealed by a birefringence modulation which rapidly builds nonlinearities. We describe how the focal conics nucleate on these nonlinearities. In Sec. IV we discuss our observations and show that the growth instability probably obeys a Mullins-Sekerka mechanism by diffusion of impurities. Finally, from the correlation of our observations, we propose that the nucleation of the focal conics occurs through a *fracture* mechanism exited by the nonlinearities of the growth instability.

II. EXPERIMENT

Our experimental setup, similar to the one of Ref. [3], may be described as follows. A liquid-crystal droplet, of typical radius $R_m \sim 1000$ μm and height $H_m \sim 100$ μm, is placed on an untreated glass holder. The material used is 10CB (4-*n*-decyl-4′-cyanobiphenyl), which presents a smectic-*A*–isotropic transition at $T_0 = 50.5\,^\circ$C. The glass holder is then laid on a heating plate regulated at $T \sim 50\,^\circ$C within ± 2 mK. To prevent air convection, we place a covering glass plate ~ 100 μm above the top of the droplet, using 200-μm Mylar spacers. The oven cover is placed well above the plates to produce a vertical temperature gradient $G \sim 1$ mK/μm on the droplet (the top of the drop is colder). Observation is made with a polarizing microscope, under crossed polars. We place the observation point halfway between the center and the borders of the droplet, at 45° from the polarizers' cross to get the maximum birefringence signal. A video camera and a video recorder are attached to the microscope. We can also add a photomultiplier to measure the local smectic-*A* plate birefringence (averaged in a $\sim 10 \times 10$ μm^2 window). Alternatively, we use a Michelson interferential lens (Ealing, 25-0084) to measure the drop profile from equal-altitude fringes. In this case the drop is illuminated by reflection using a mercury lamp with a green filter (5460 Å).

III. RESULTS

We start the experiment by placing the drop in the isotropic phase; we then decrease the temperature. A smectic plate in contact with the isotropic phase nucleates from the top of the droplet. Observed between crossed polars, this plate shows a black cross, the usual conoscopic pattern of a uniaxial crystal's normal section. From this we deduce that the smectic layers grow parallel to the air interface. The smectic thickness $h(t)$ is estimated from the birefringence measured by the photomultiplier. The growth velocity $V = \partial h/\partial t$ can be approximately adjusted in the range $V \sim 5$–50 μm/s.

For $V > V_c \sim 25$ μm/s, we observe the onset of a concentric wave pattern corresponding to a birefringence modulation of period $\lambda \sim 20$ μm (Fig. 1). We can suppress the waves by lowering the velocity or even inverting the growth direction (melting), i.e., this phenomenon is reversible. The waves appearing during the smectic growth do not drift. We interpret the onset of this wave pattern as a *growth* instability. This instability looks supercritical as the waves seem to appear with an infinitesimal amplitude, but our present accuracy does not allow us to demonstrate it quantitatively.

As the smectic liquid crystal grows, the wave pattern builds a sequence of optically revealed nonlinearities (Fig. 1). First, the wave pattern transforms into a system of equidistant bands with the same period, as if one "sign" of the wave modulation was amplified and the other reduced. At the same time, as the instability amplitude increases, a well-defined separation line appears along the center of these bands. It corresponds to a steep birefringence variation from one side of the line to the other (see Fig. 2). With respect to the background birefringence, the part of these bands closer to the drop center (the "inner" part) shows a lack $(-)$ of birefringence and the opposite part (the "outer" part) shows a birefringence excess $(+)$. Let us call this a $\{-,+\}$ birefringence radial polarity. As the instability goes on developing, these bands are subject to peristaltic secondary modulations which build individual "spindles." The transformation of the bands into spindles looks very similar to the Rayleigh instability of a liquid cylinder which starts breaking into a system of separated droplets. These spindles also show a well-defined $\{-,+\}$ polarity, always pointing toward the center of the drop as for the "mother" bands.

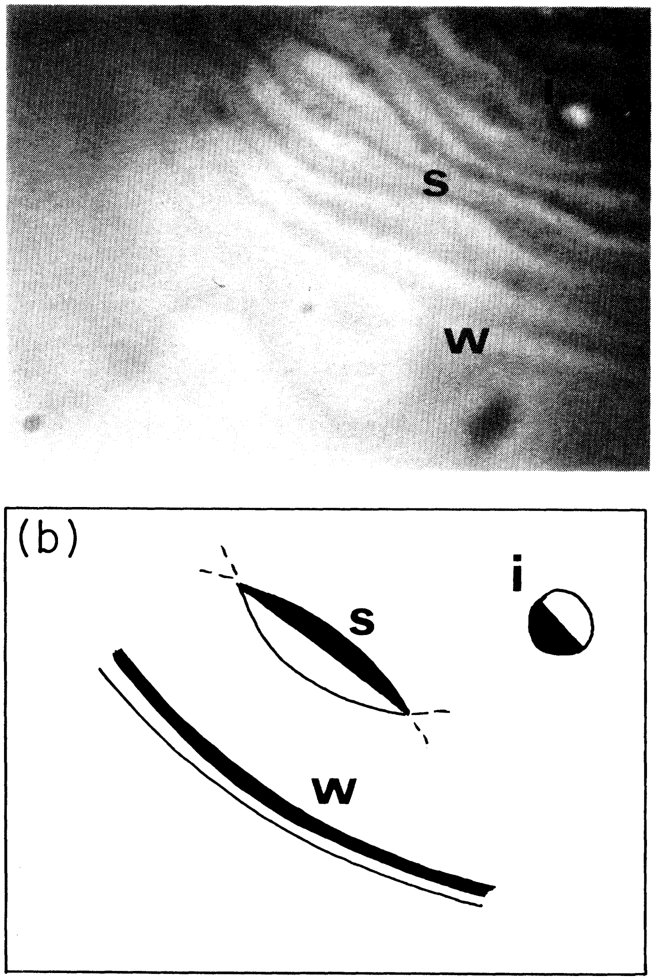

FIG. 1. (a) The dynamical birefringence concentric waves (w) and their nonlinearities: spindles (s) and islands (i). The distance between the waves is ~ 20 μm. The drop center is located at the upper-right corner and the observation is made at 45° from the polarizers' cross. The spindles show a $\{-,+\}$ birefringence polarity and the islands a strong opposite $\{+,-\}$ white-black birefringence polarity. (b) Schematic drawing of the waves' nonlinearities.

Some spindles remain more or less steady in size, while the other ones become even more nonlinear and give birth to new circular structures. We observe two characteristic behaviors. (i) Some small spindles become more or less circular and drift slowly away from the droplet center, before vanishing. They still show a faint $\{-,+\}$ radial polarity. (ii) Alternatively, the birefringence of the outer part $(+)$ of a large spindle increases violently and transforms into a circular birefringent structure, drifting now swiftly toward the center. It becomes a circular "island" showing a strong but opposite $\{+,-\}$ polarity (Fig. 1). Typically, close to the droplet center, these islands of diameter $\sim 5-20$ μm are black and white on a gray background. It occurs that two islands meet; they coalesce and build a bigger island. The big islands tend to become perfectly circular and show a sharp outline. As they arrive at the droplet center, they lose their birefringence polarity. Such symmetric islands look very much like the well-known disks corresponding to a quantized number of smectic layers. Note that all these island

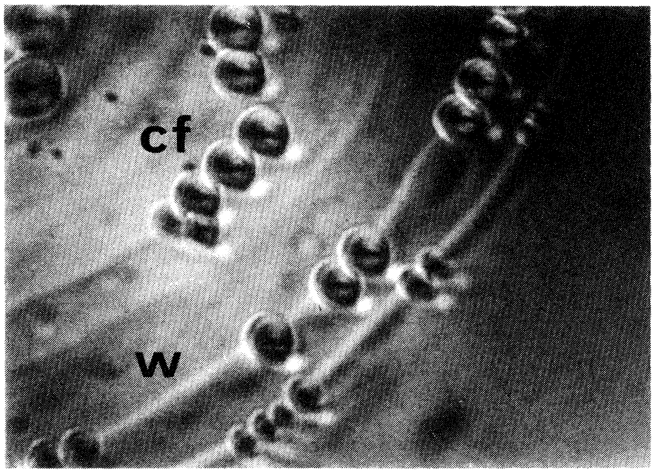

FIG. 2. Rows of focal conics (cf) nucleating along concentric nonlinear waves (w) appearing as bipolar bands. The bands show a strong $\{-,+\}$ yellow-red (gray-black on the picture) birefringence polarity. The drop center lies below the upper-left corner.

appear continuously from the growth of the wave pattern, and not from a possible but not observed coalescence of independent Grandjean "bâtonnets" with the smectic plate.

When the nonlinearities (bands, spindles, or islands) are well developed, they suddenly give birth to *focal-conic* defects, appearing as individual circular domains of radius r. The origin of these focal conics is already known [3] and will be recalled later; we are interested here in their nucleation mechanism. We observe nucleation of a large number of focal conics. The nucleation follows a very reproducible law, which depends on the type of nonlinearity involved: In the case of a $\{-,+\}$ band or spindle, the nucleation point is located in the outer part, somewhere between the central separation and the outer border [Figs. 2 and 3(b)]; in the case of a $\{-,+\}$ island, the nucleation point is located exactly on the outline of the island, at the point which is the nearest to the center of the smectic droplet [Fig. 3(b)]. Finally, the focal conics nucleating on a large disklike island (at the drop center) appear simultaneously all around its steep outline (Fig. 4). When the disklike island is much larger than the equilibrium size of the focal conics, the latter often gather at the center of the island. As they nucleate, the focal conics grow during a time ~ 100 ms, from a small size under the resolution limit to an equilibrium size $r_e \sim 10$ μm depending on the plate thickness h. As described in Ref. [3], the focal conics finally gather in a hexagonal array floating freely inside the smectic plate, close to the center of the drop. When h reaches the drop height H_m, the array touches the glass holder and simply remains steady.

Switching off the transmission light, we can measure the profile $H(R)$ of the drop free surface with the Michelson objective (Fig. 5). At first, as the drop is in the isotropic phase, we observe a system of large circular interference fringes from which we can deduce the curvature radius ρ of the droplet. Measuring the droplet parameters R_m and H_m, we have verified that ρ is $\sim(R_m^2+H_m^2)/2H_m$ which means that the drop can be assimilated to a portion of a sphere. During the growth, we detect the birefringence waves by simply restoring the transmission light. We find that the circular fringes of the drop-air surface are not modified by the presence of a nonlinear wave pattern, i.e., there is no free-surface image associated to the waves, the bands, or the spindles. However, when a well-developed island appears, we observe above it a free-surface bump of order $\delta H \sim +1500$ Å (one half fringe). Later on, when the focal conics appear, we observe above each one a set of circular fringes corre-

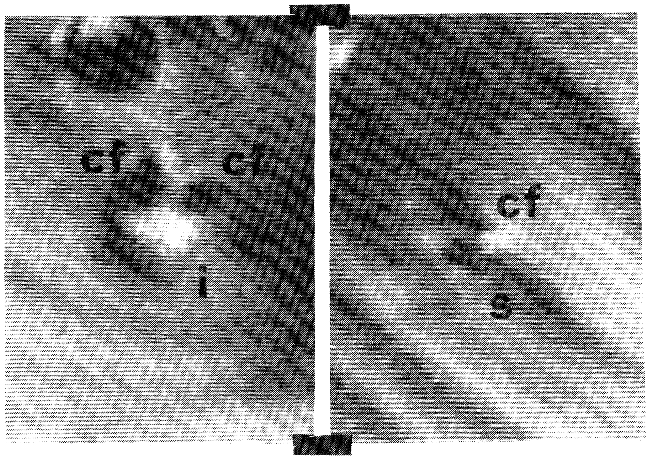

FIG. 3. Nucleation of the focal conics (cf): (a) on the outline of an island (i) toward the drop center; (b) between the center and the outer part of a large $\{-,+\}$ yellow-red (gray-black on the picture) spindle (s). Photo (a) is a magnified view of the island of Fig. 1 delayed ~ 20 ms.

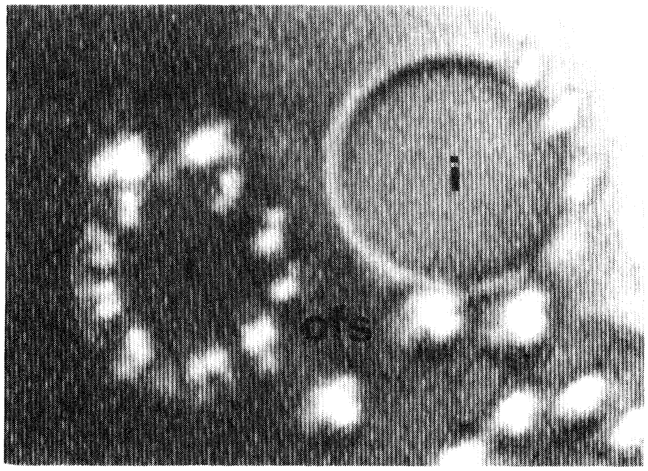

FIG. 4. Nucleation of the focal conics (cfs) all around the steep outline of symmetric disclike islands (i).

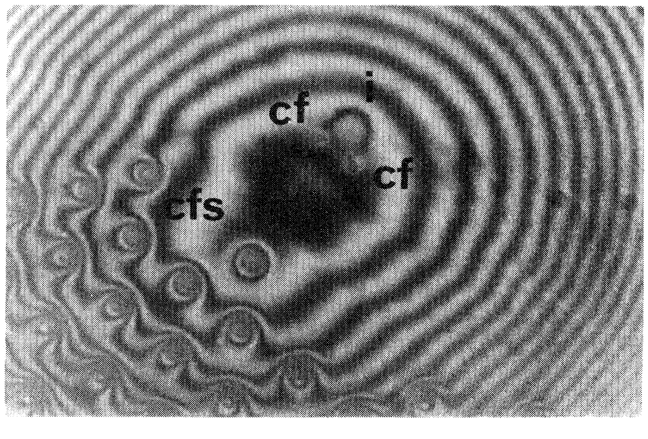

FIG. 5. Michelson interferometer image of the drop free surface showing the nucleation of focal conics (cfs) from a drifting island (i). Only the drop free-surface profile is visible on this picture, not the bulk birefringence. The focal conics are materialized by their free-surface depressions (concave perturbations to the central fringes). Although it is not clear on this micrograph, the island image is a free-surface bump (convex perturbation to the central fringes). Here the thermal gradient is not exactly vertical so that the equilibrium focal-conic network is shifted from the drop center.

sponding to a free-surface depression of a few micrometers. As a typical example, Fig. 5 is the free-surface image of the birth of focal conics from an isolated island drifting toward the droplet center.

IV. INTERPRETATION

Let us first recall why the free-floating focal conics are stable [3]. Initially, the smectic layers growing parallel to the air interface are also almost parallel to the isotropic interface. This involves a smectic-A–isotropic surface energy $\gamma_{\parallel}$ significantly larger than $\gamma_{\perp}=\gamma_{\parallel}-\Delta\gamma$ corresponding to the perpendicular orientation. The focal conics are stable because they set the preferred perpendicular orientation of the layers at the interface, with a minimal bulk distortion energy (Fig. 6). The free-surface depression associated to a focal conic is due to the competition between the air-surface tension and the rigidity of the layers which try to remain equidistant. Quantitatively, the excess free energy associated with a cylindrical focal-conic domain of radius r inside the smectic plate of thickness h is written [3]

$$\delta F(r,h)=\alpha Kr+\beta Kh-\Delta\gamma\pi r^2+\cdots , \qquad (1)$$

where the ellipsis represents higher-order terms. The first two terms, corresponding to the focal-conic texture plus the disclination line energy, are linear (α,β dimensionless). The third term, describing the surface-energy gain, is quadratic and stabilizes the domain as soon as $r>(r_0 h)^{1/2}$, where $r_0\sim K/\Delta\gamma$. The last term describes the saturation effects defining the equilibrium value $r_e(h)$ of the grown focal conics. One such term is the excess energy associated to the air free-surface depressions above the focal conics. Typical values for 10CB are $K\sim 10^{-6}$ cgs for the splay elastic constant and $\Delta\gamma\sim 0.05$ erg/cm^2 giving $r_0\sim 2000$ Å. According to Ref. [3], the focal conics are metastable as soon as $r>r_0$. It is therefore enough to create a submicrometer focal conic to pass the nucleation barrier.

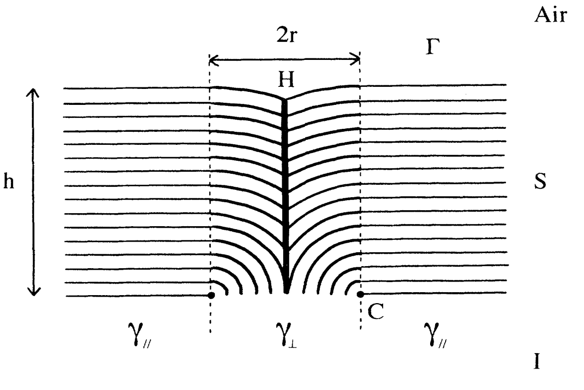

FIG. 6. Principles of the focal-conic static instability. With a minimal bulk distortion energy $\sim Kr+Kh$, the focal conics relax the smectic-A–isotropic surface energy anisotropy $\sim(\gamma_{\parallel}-\gamma_{\perp})r^2$. The equilibrium radius $r_e(h)$ of the focal conics is determined by the saturation due to the free-surface depression. This first-order textural instability is described in Ref. [3].

Before discussing the growth instability mechanism, let us first examine the origin of the birefringence modulation. We can deduce from the absence of free-surface image associated with the waves, that the birefringence modulation is due to an undulation of the smectic-A–isotropic interface (the smectic layers remaining uniformly parallel), rather than a bulk undulation of the layers. Indeed, the air-surface tension would not be strong enough to quench such an undulation, as shown by the following arguments. Assume a bulk layer undulation of wavelength a and amplitude $a\alpha$. In an infinite medium, it would relax on a length [5] $H_{\infty}\sim a^2/\lambda_p \gg a$, where $\lambda_p=(K/B)^{1/2}$ is of order 30 Å, $B\sim 10^8$ cgs being the layer dilation modulus. Assume now that this layer undulation is quenched on a length H_m. Let us compare the dilation energy per surface unit $B(a\alpha/H_m)^2 H_m$ with the air-surface energy excess associated with an undulation of the air free surface with an angle α, i.e., $\Gamma\alpha^2$, $\Gamma\sim 25$ cgs being the air-surface tension. Since Γ/B is expected to be also of order λ_p (a molecular length), the ratio measuring the relative "strength" of the free surface is $\sim H_m/H_{\infty}$. With $a\sim 10$ μm, we find $H_{\infty}\sim 3\times 10^4$ μm giving $H_m/H_{\infty}\sim 3\times 10^{-3}$, which justifies the proposition. The origin of the islands' free-surface bumps will be discussed later.

From the preceding argument, the growth instability appears very similar to a Mullins-Sekerka instability [6,7]. In liquid crystals, this type of instability has been studied at the nematic-isotropic interface [8], and at the smectic-A–smectic-B interface [9]. When the growth velocity is limited by the diffusion of impurities in the liquid phase, the Mullins-Sekerka model predicts that the interface is unstable above a velocity threshold

$$V_c\sim\frac{DG}{m\Delta c}\ , \qquad (2)$$

where $D\sim 5\times 10^{-5}$ cm^2/s is a typical impurity diffusion coefficient [8], $G\sim 1$ mK/μm is the thermal gradient, $m\sim 100$ K is the "liquidus" slope, and $\Delta c\sim 10^{-4}$ the assumed smectic-A–isotropic miscibility gap. With these values we obtain $V_c\sim 50$ μm/s which is compatible with our observations.

Our experimental accuracy is not high enough to investigate the appearing instability wavelength near the threshold V_c. In most experiments, V is typically a factor of 2 above threshold. Therefore, taking $V\sim 2V_c$, the appearing wavelength must be compared with the fastest growing wavelength

$$\lambda_f\sim\left[\frac{(2\pi)^2\gamma_{\parallel}v_m}{(\Delta_c)^2\dfrac{\partial\mu}{\partial c}}\right]^{1/2}\left[\frac{D}{2V_c}\right]^{1/2}\sim d_{\mathrm{ch}}^{1/2}l_T^{1/2}\ , \qquad (3)$$

whose expression is valid both in the subcritical regime and the supercritical regime *above* threshold. l_T written in (3) as $D/2V_c$ and classically defined by $m\Delta c/G$ ($\sim D/V_c$) is the thermal length. d_{ch} is the chemical capillary length. Formula (3) differs from $\lambda_c\sim d_{\mathrm{ch}}^{1/3}l_T^{2/3}$ giving the critical wavelength appearing *at* the threshold $V=V_c$ [7], which was used to demonstrated experimentally the supercritical behavior of growing nematics [8].

In (3), $c \sim 10^{-3}$ is the assumed fraction of impurities, μ is the chemical potential of the impurities, and $v_m \sim 7.5 \times 10^{-22}$ cm^3 a typical molecular volume. Assuming also $\gamma_\parallel \sim kT/\xi^2$ ($\xi \sim 200$ Å is the smectic-A–isotropic coherence length) and $\partial\mu/\partial c \sim kT/c$, we obtain with $V \sim 2 \times 25$ μm/s the previously given $\lambda_f \sim 30$ μm, which is compatible with our observations.

Let us now try to explain the *optical contrast* of the interfacial distortions. Since the smectic layers do not undulate, only the modulations δh of the smectic plate thickness can contribute to the birefringence modulation. However, one must take into account the *refraction* at the smectic-A–isotropic interface to describe the bipolar birefringence of the bands, spindles, and islands. Let the local interface normal be tilted with an angle ϕ with respect to the vertical z axis, and θ be the angle between the molecules (normal to the smectic layers) and the z axis (Fig. 7). The extraordinary beam is locally refracted by an amount $\delta\phi$ which must satisfy $n_i \sin\phi = n_s \sin(\phi + \delta\phi)$, where n_s can be approximated by $n_o + \Delta n \sin^2(\theta - \delta\phi)$, $\Delta n = n_e - n_o$ being the difference between the smectic extraordinary and ordinary indices, and $n_i \sim n_o + \Delta n/3$ the refractive index of the isotropic phase. A good approximation of the refraction angle is ($\Delta n/n_o \ll 1$)

$$\delta\phi \sim \frac{\Delta n}{n_o}\left(\tfrac{1}{3} - \sin^2\theta\right)\tan\phi \; . \tag{4}$$

The birefringence modulation is defined as the comparison between the path differences (between the extraordinary and ordinary rays) across a wave or inside and outside a nonlinearity, i.e., $(h + \delta h)\Delta n \sin^2(\theta - \delta\phi) - h\Delta n \sin^2\theta$. It has two contributions; one is due to the refraction effect ($\delta\phi$) and the other one comes directly from the thickness variation (δh). The ratio between them is $x \sim (h\delta\phi)/(\delta h \frac{1}{2}\tan\theta)$. Using Eq. (4) and assuming $\theta \ll 1$, we obtain

$$x \sim \frac{4}{3}\frac{\Delta n}{n_o}\frac{h}{a\theta} \; , \tag{5}$$

where $a \sim 2\delta h/\tan\phi$ is the size of the linear or nonlinear object. x is independent of the modulation amplitude δh. The values $n_o \sim 1.5$, $\Delta n \sim 0.2$, $\theta \sim 10°$ are typical of the smectic and the observation point. Conversely, a and h are characteristic of the interfacial object. For the waves h is small ($h \sim 10$ μm) and a is large ($a \sim 20$ μm) which results in $x \sim 0.5$. For the waves the usual thickness effect dominates. For the bands, which correspond to more developed waves, up to the spindles and the islands, h is larger ($h \sim 50$ μm) and a smaller ($a \sim 10$ μm), then x is ~ 5 which means that the refraction effect dominates. Reobserving carefully the transition from the waves to the bands, one does see the $\pi/2$ phase shift of the optical birefringence contrast toward the drop center, since the thickness effect measures the *amplitude* modulation and the refraction effect the *slope* modulation. From the experimental sign of the shift, we deduce that the bands are localized smectic "holes." Therefore the $\{-,+\}$ polarity reveals the top of smectic holes. This correspondence simply results from the refraction effect (Fig. 7): θ being small, the smectic refractive indices are smaller than n_i, and the light rays diverge on a smectic "bulge" or converge on a smectic hole. At this point, we shall assume that the interface is more or less horizontal since it is imposed by the thermal gradient. Then, as the layers grow parallel to the drop surface, they are naturally tilted with respect to the isotropic interface, and therefore the refraction has the following effect: it increases the birefringence on one side of the nonlinearity and reduces it on the other side. The sign of this birefringence polarity depends on whether the nonlinearities are bulges or holes: a $\{-,+\}$ polarity reveals the top of a smectic hole and the opposite $\{+,-\}$ polarity the top of a smectic bulge. This agrees with our previous observation on the bands. The spindles coming continuously from the bands must also be holes. Using this polarity law, we deduce that the circular islands are smectic bulges. Assuming a grown bulge with $\phi \sim 45°$, i.e., $\delta h \sim a/2$, the amplitude of the birefringence modulation is $\sim \frac{4}{3}(\Delta n/n_o)(\delta h\theta/a)h\Delta n \sim 1500$ Å with the values previously given. This corresponds indeed to the observed modulation of the central islands (black and white on a gray background).

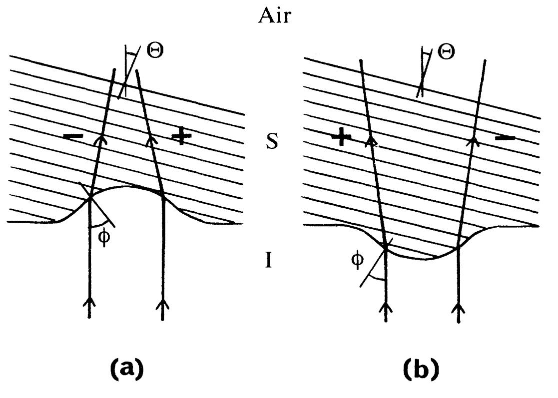

FIG. 7. Refraction contribution to the integrated birefringence induced by smectic hole (a) and smectic bulge (b) nonlinearities. A birefringence polarity is induced since the angle between the light rays and the normal to the layers is increased on one side of a nonlinearity and reduced on the other side. Referring first to the sign toward the drop center (on the left), smectic holes show a $\{-,+\}$ birefringence polarity and smectic bulges the opposite $\{+,-\}$ polarity. Close to the drop center and for well-developed nonlinearities, this unusual contribution to the birefringence dominates the usual thickness variation contribution.

We now come back to the origin of the free-surface bumps. We have observed that above a well-developed island, the smectic layers are bent. From the static mechanism which stabilizes the grown focal conics, we can expect this bend to come from a torque acting at the isotropic interface (Fig. 8). Let us verify that the interfacial anisotropy can produce such an effect. We describe the smectic-A–isotropic surface energy by $\gamma = \gamma_\parallel - \Delta\gamma \sin^2(\theta - \phi + \alpha)$, $\theta - \phi$ being the layer-surface angle and α the small bend angle. Assuming $\theta - \phi \sim 45°$ for a

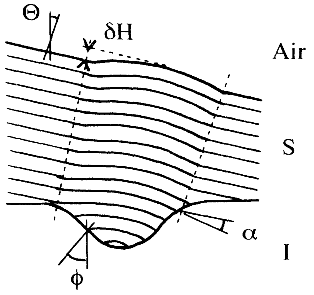

FIG. 8. Bulge-induced smectic layers bending toward the preferred perpendicular orientation at the isotropic interface. This relaxation can explain the small free-surface bumps ($\delta H \sim +1500$ Å) associated to well-developed islands (cf. Fig. 5).

grown bulge, the energy gain associated to a bend angle α is $\sim a^2\Delta\gamma\alpha$. Since the free surface does not quench the perturbation, this energy must be balanced with the corresponding free-surface energy excess $\sim a^2\Gamma\alpha^2$. Comparing these two terms, the bump $\delta H \sim a\alpha$ is expected to be $\sim a(\Delta\gamma/\Gamma) \sim 200$ Å, which order of magnitude agrees with our observations. Note that the width of the bump should be comparable with the width of the bulge: Indeed a local perturbation of the smectic layers is known to propagate normally to the layers, the deformation being located inside a narrow paraboloid [10] of width $\Delta x \sim (2z\lambda_p)^{1/2}$. With $a \sim 10\ \mu$m and $\lambda_p \sim 30$ Å, we obtain $\Delta x \sim 0.2\ \mu$m, indeed $\ll a$. In the case of small waves, as $\theta - \phi \ll 1$, the energy gain $\sim a^2\Delta\gamma\alpha^2$ becomes quadratic and is always too small to create the layer bending since $\Delta\gamma \ll \Gamma$. This explains quantitatively the absence of any image associated to the waves. As for the spindles, they are probably not enough developed to induce an elastic image.

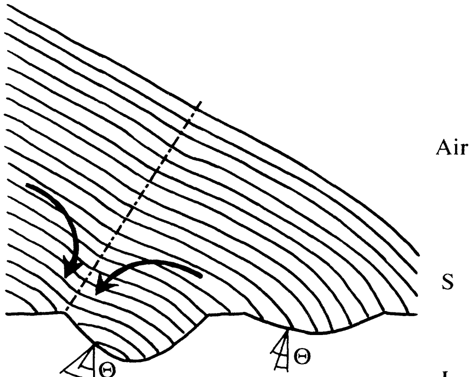

FIG. 9. Fracture mechanism on a well-developed bulge. When the bulge inclination ϕ is greater than the smectic layers' tilt θ, the layers are notched by the isotropic interface. The layer bending pattern induces then a pricking fracture which has the very symmetry of a focal conic. The nucleation point (notch) is located on the outline of the bulge toward the drop center (left side).

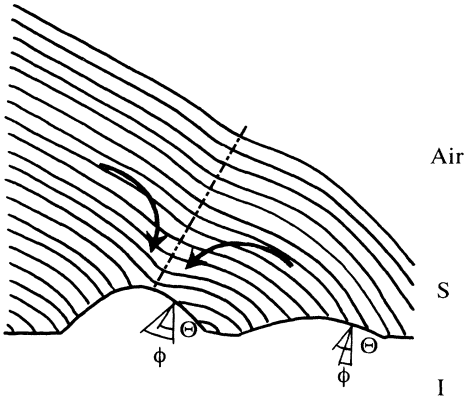

FIG. 10. Pricking fracture on a well-developed hole. The mechanism is the same as for a bulge (cf. Fig. 9) but the nucleation point (notch) is located near the center of the hole, more precisely between the hole center and the hole outer part away from the drop center (right side).

Finally, from the effect of the layer bending on a hole or a bulge at the isotropic interface, we can propose the following *fracture* mechanism for the focal-conic nucleation (Figs. 9 and 10). At a given point, the tilt θ of the smectic layers is fixed. When a hole or a bulge grows, the local interface inclination ϕ increases. When ϕ is still less than θ, the bending pattern does not change the smectic plate's symmetry. For $\phi > \theta$, a number of smectic layers become *notched* by the isotropic interface. Close to this notch, the layers bend now in opposite directions: the bending pattern looks like a pricking fracture which has the very symmetry of a focal conic. It is straightforward to see that the weak point of this fracture is located on the outline of the bulges toward the drop center (Fig. 9), or in the middle of the holes (Fig. 10). Since we already know that spindles and nonlinear waves are holes and that islands are bulges, our observations are coherent with this fracture mechanism. Note that in the case of the large disclike islands (cf. Fig. 4), the smectic layers are probably notched all around their sharp outline.

V. DISCUSSION

It would be interesting to study in more detail the growth instability itself, and to check, for instance, the fracture threshold condition $\phi > \theta$. However, the birefringence being a function of both the wave profile and its spatial derivative, the resolution required for such studies is rather high, $\sim 1\ \mu$m spatially and ~ 20 ms for the time resolution (one video frame). This exceeds our present capability. The standard geometry of Ref. [8] seems better adapted; however, some additional difficulties would probably arise from the interaction of the smectic layers with the lateral bounding plates (absent in our geometry).

From the symmetry of the smectic phase, whose layers are tilted with respect to the interface, we would expect the waves to drift radially. In a Mullins-Sekerka mechanism, the drift velocity should be proportional to the impurity gradient inside the smectic and to the layer inclination α at the interface. We do not observe any significant drift. This is probably difficult to observe as (i) α is small, (ii) the observed $\pi/2$ phase shift in the wave contrast gives an apparent $\lambda/4$ drift toward the center, and (iii) the rapid onset of the focal conics shortens the available observation time. As for the drift of the islands and circular spindles, it is probably rather difficult to model. Indeed a dynamical mechanism should be nonlinear since the drift direction depends on whether the nonlinearities are bulges or holes. We also cannot exclude a possible static drift mechanism due to the bending pattern, which is asymmetric (see Fig. 8).

Finally, the propagation of the fracture itself is interesting to study. In fact, in a lateral geometry we have observed the onset of the central line of a focal conic, from an interfacial perturbation. The dynamical study of such a fracture, requiring a high-resolution temporal experimental setup, is beyond the scope of the present work.

VI. CONCLUSION

In this work, we have resolved the sequence of instabilities occurring during the growth of a smectic-A plate inside the isotropic phase in a free drop geometry. Before the focal-conic *static* instability already known [3], we have observed an interfacial *growth* instability which probably obeys a Mullins-Sekerka mechanism by diffusion of impurities. We have focused our attention on the nucleation of the "static" focal conics, occurring on the nonlinearities of the growth instability. To explain the nucleation process, we have proposed a fracture mechanism. The larger dynamical distortions of the smectic-A–isotropic interface *notch* the smectic layers. The cut smectic layers bend in opposite directions around these notches, to relax the surface-energy anisotropy. This bending pattern, which has the very symmetry of a focal conic, is likely to induce a linear *pricking fracture*, precursor of a focal conic. Our model is based on the observed location of the focal-conic nucleation point, which is different for the various types of nonlinearities. The link between the two instabilities is now clear: The dynamical instability helps the smectic texture to tunnel through the potential barrier of the focal-conic static first-order instability.

---

*Permanent address: Laboratoire de Dynamique et Structure des Matériaux Moléculaires. Université de Lille 1, F-59655 Villeneuve d'Ascq, France.

[1] P. G. de Gennes, *The Physics of Liquid Crystals* (Academic, New York, 1974).
[2] G. Friedel and F. Grandjean, Bull. Soc. Fr. Mineral. **33**, 409 (1910).
[3] J. B. Fournier, I. Dozov, and G. Durand, Phys. Rev. A **41**, 2252 (1990).
[4] J. B. Fournier and G. Durand, J. Phys. (Paris) II **1**, 845 (1991).
[5] G. Durand, C. R. Acad. Sci. 275 (1972).
[6] W. W. Mullins and R. F. Sekerka, J. Appl. Phys. **35**, 444 (1964).
[7] J.S. Lander, Rev. Mod. Phys. **52**, 1 (1980).
[8] P. Oswald, J. Bechhoefer, and A. Liebchaber, Phys. Rev. Lett. **58**, 2318 (1987).
[9] F. Melo and P. Oswald, Phys. Rev. Lett. **64**, 1381 (1990).
[10] P. G. de Gennes, C. R. Acad. Sci. **275**, 939 (1973).

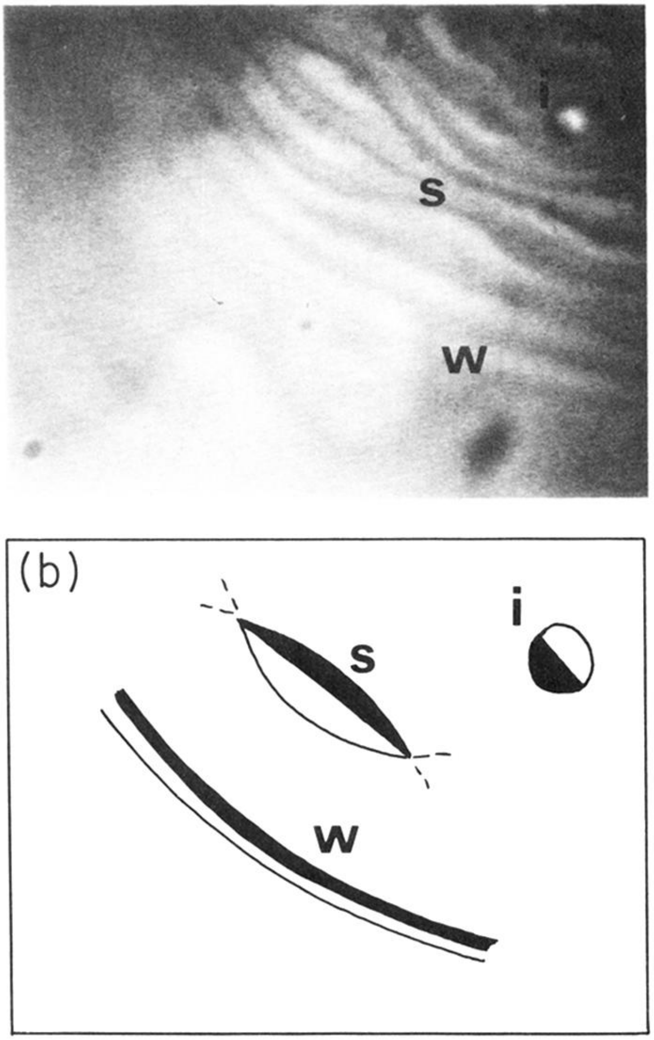

FIG. 1. (a) The dynamical birefringence concentric waves (w) and their nonlinearities: spindles (s) and islands (i). The distance between the waves is $\sim 20\ \mu$m. The drop center is located at the upper-right corner and the observation is made at 45° from the polarizers' cross. The spindles show a $\{-,+\}$ birefringence polarity and the islands a strong opposite $\{+,-\}$ white-black birefringence polarity. (b) Schematic drawing of the waves' nonlinearities.

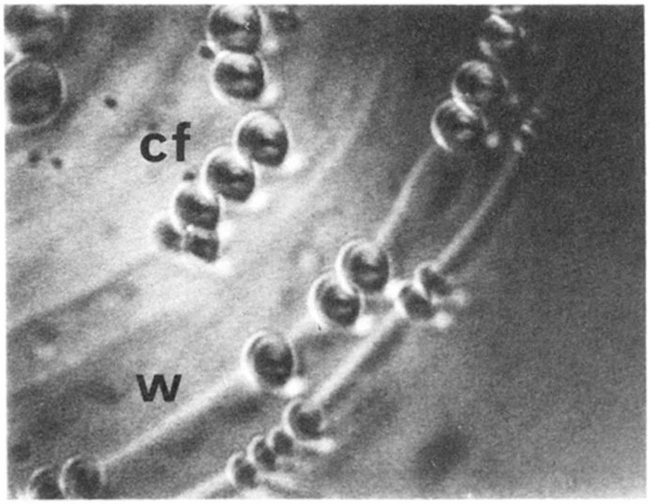

FIG. 2. Rows of focal conics (cf) nucleating along concentric nonlinear waves (w) appearing as bipolar bands. The bands show a strong $\{-,+\}$ yellow-red (gray-black on the picture) birefringence polarity. The drop center lies below the upper-left corner.

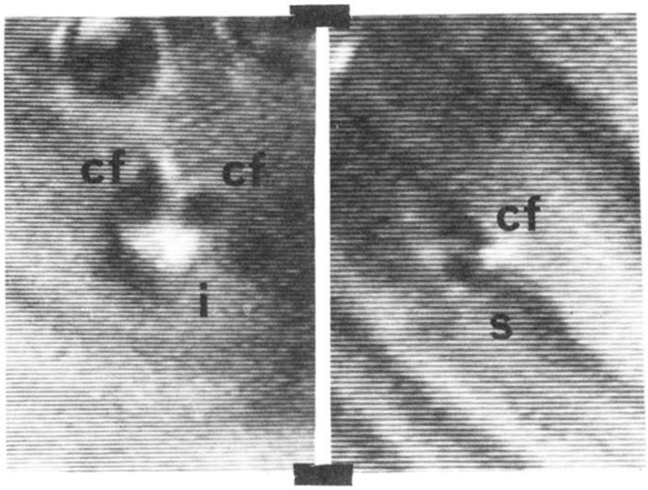

FIG. 3. Nucleation of the focal conics (cf): (a) on the outline of an island (i) toward the drop center; (b) between the center and the outer part of a large $\{-,+\}$ yellow-red (gray-black on the picture) spindle (s). Photo (a) is a magnified view of the island of Fig. 1 delayed ~20 ms.

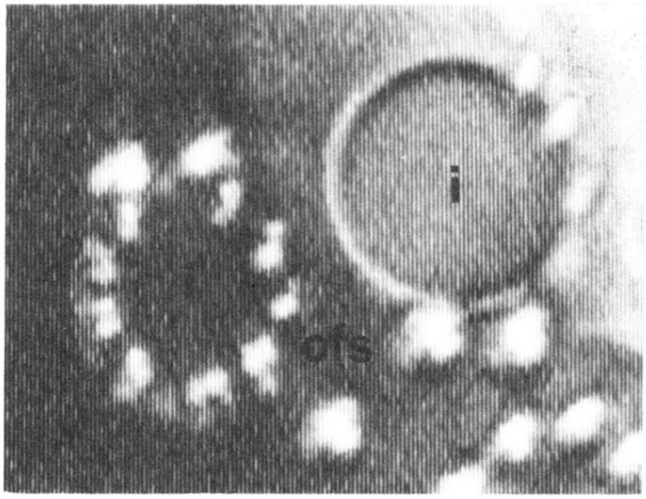

FIG. 4. Nucleation of the focal conics (cfs) all around the steep outline of symmetric disclike islands (i).

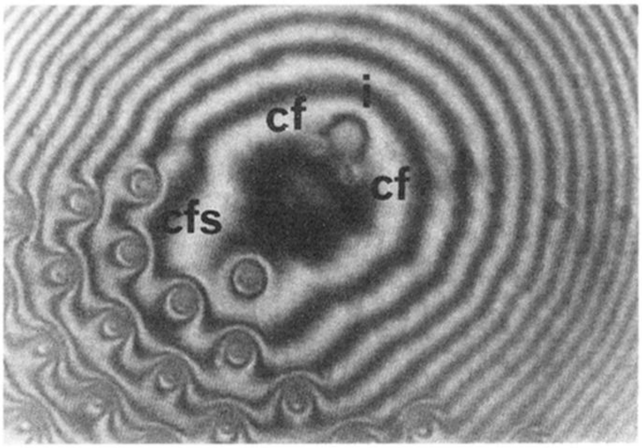

FIG. 5. Michelson interferometer image of the drop free surface showing the nucleation of focal conics (cfs) from a drifting island (*i*). Only the drop free-surface profile is visible on this picture, not the bulk birefringence. The focal conics are materialized by their free-surface depressions (concave perturbations to the central fringes). Although it is not clear on this micrograph, the island image is a free-surface bump (convex perturbation to the central fringes). Here the thermal gradient is not exactly vertical so that the equilibrium focal-conic network is shifted from the drop center.